Phase-matched second-harmonic generation in slow-light photonic crystal waveguides

Sina Saravi,* Séverine Diziain, Matthias Zilk, Frank Setzpfandt, and Thomas Pertsch
Institute of Applied Physics, Abbe Center of Photonics, Friedrich-Schiller-Universität Jena, Max-Wien-Platz 1, 07743 Jena, Germany
(Received 7 September 2015; published 11 December 2015)

We present an analytical description of phase-matched second-harmonic generation in photonic crystal waveguides in the presence of loss. In particular, we investigate the case where the second-harmonic modes suffer from radiative losses. We use the adjoint field formalism to develop a coupled-mode theory that uses the quasinormal Bloch modes as the basis for modal expansion. To test our analytical description numerically, we propose a design in a lithium niobate photonic crystal slab waveguide, where a slow-light mode at the fundamental harmonic frequency is phase matched to a leaky mode at the second-harmonic frequency. The results of the numerical experiment agree with our analytical predictions.

DOI: 10.1103/PhysRevA.92.063821 PACS number(s): 42.70.Qs, 42.65.Ky, 42.70.Mp, 42.82.Et

I. INTRODUCTION

Photonic crystal (PC) devices are suitable platforms for fully integrated optical signal processing since they provide control over the flow of light on the subwavelength scale [1]. In particular, PC slab waveguides (PCSWs), shown schematically in Fig. 1, are suitable for achieving strong control over the dispersion relation of electromagnetic modes since by altering the dispersion relation of modes and lowering their group velocity to obtain slow light, smaller photonic devices and more efficient nonlinear interactions can be obtained [2–4]. The latter is possible since light in a slow mode has, for the same optical power, a higher intensity than in a regular guided mode. As a result, nonlinear interactions, which by nature are intensity dependent, become enhanced and more efficient. This makes slow light PCSWs particularly interesting for integrated light sources based on nonlinear parametric processes, such as second-harmonic generation (SHG) [5,6], third-harmonic generation (THG) [7,8], and four-wave mixing (FWM) [9].

The first requirement for a parametric process is the conservation of energy. In terms of this aspect, parametric processes in PCSWs can be placed in two categories. The first category includes processes that involve photons with close frequencies, e.g., a FWM process, where all the four waves involved in the process are around the frequency of the slow mode to benefit from its enhancement effect [9]. The slow-light mode is designed to be under the light line and inside the band-gap frequency range of the PC slab and therefore is ideally lossless. Standard coupled-mode theory involving lossless Bloch modes can be used for analytical investigation of such a process [10,11]. The second category includes processes that involve photons of very different frequencies, such as SHG and THG. To benefit from slow light, the fundamental-harmonic (FH) frequency is chosen to coincide with the slow mode. However, the second-harmonic [5,6] (SH) or the third-harmonic [7,8] frequencies are usually above the light line. This means that the modes of the waveguide at the higher-harmonic frequencies couple to the radiation modes, which leads to energy loss. For such leaky [12] modes the theories involving lossless modes cannot in general be applied to analytically investigate light propagation. Although SHG has been investigated for two-dimensional (2D) planar PCs [13], the treatment is not applicable to PCSWs with leaky modes, as in the 2D case the structure is assumed to be z invariant, hence the effect of the light line is ignored and the theory is only developed for the lossless modes of the z-invariant system.

The second requirement for a parametric process is the conservation of momentum, i.e., the need for phase matching between the modes. For the first category of processes where frequencies of the modes involved are close to each other, e.g., FWM, achieving phase matching is a relatively simple task, compared to the second category with SHG and THG. Especially if there is only one mode of operation in FWM for all the four waves involved [9], then phase matching is ensured naturally. However, for the SHG and THG, due to the strong material and modal dispersion, achieving a phase-matched interaction is not as simple. Because of the lack of structure designs for phase-matched processes, in the experiments done to date on THG and SHG in PCSWs the slow FH mode generated the higher-harmonic signal directly into the continuum of the radiation modes, which was detected from above. In this way, the higher-harmonic field does not propagate with the guided FH mode and is immediately lost, which is the main reason that phase matching cannot take effect [14]. Although the non-phase-matched process allows for a more wideband nonlinear interaction, it is less efficient compared to one that is phase matched. For an efficient phase-matched interaction to take place, the leaky SH mode has to be concentrated in the waveguide region and have a long decay length. Finding such modes adds to the complexity of the design. Once again, designs are available for phase-matched SHG in planar PCs with finite slab thickness [15], but not for PCSWs.

Arbitrary phase matching could be achieved by using the quasi-phase-matching technique [16,17]. However, this technique has not yet been implemented in PCSWs and is limited to specific material systems. Our aim is to achieve modal phase-matching purely through the dispersion of the guided modes, which does not rely on any additional technology besides the structuring necessary to realize the photonic crystal.

In this work we address the lack of both a phase-matched design and an analytical description for the specific case of SHG in PCSWs. It is important for both issues to be

*sina.saravi@uni-jena.de

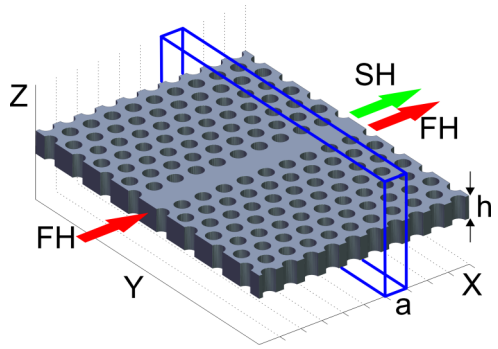

FIG. 1. (Color online) Schematic of the guided second-harmonic generation in a photonic crystal slab waveguide, with slab thickness h, hole radius R, and lattice constant a. Here FH and SH stand for the fundamental- and the second-harmonic fields, respectively. The blue lines mark the edges of the supercell, which is the unit cell of the PCSW structure. It is a volume with the length of one period in the propagation direction and an infinite cross section.

addressed at the same time because for numerical investigation of the validity of the analytical description, one requires a realizable design to perform the rigorous nonlinear simulation and potentially an experiment. For the analytical description we use the adjoint reciprocity theorem as a starting point, which has already been developed as a general formalism and has been used specifically to describe cross- and self-phase modulation in metamaterials with material loss or gain [18]. We combine this formalism with the concept of quasinormal Bloch modes [19] (QNBMs), which is needed for correctly normalizing the leaky Bloch modes.

For the structure design, we choose lithium niobate ($LiNbO_3$) as the material because of its strong second-order nonlinearity, wide transparency window, and the possibility of periodic poling, which makes $LiNbO_3$ PCs an ideal platform for integrated optical devices. Recent advances in $LiNbO_3$ nanostructuring technologies [20,21] have already allowed for the realization of PC cavities [22] and integrated nanowaveguides [23,24] for SHG. Henceforth, realizing a slow-light PCSW with the required nanostructuring precision is not out of reach. In our design, a leaky SH mode of the PCSW is phase matched to a dispersion engineered slow FH mode.

Our analytical model allows us to quantitatively study the effects from phase matching, leakage, and group index on the efficiency of SHG involving a leaky Bloch mode. Most notably, we find that for the leaky mode the efficiency depends on the absolute value of the complex group index of the mode. Furthermore, the proposed design is shown to result in a narrow phase-matching bandwidth due to the strong wavelength dependence of the wave number of the slow-light mode. Finally, a nonlinear finite-difference time-domain (FDTD) simulation is performed and its result is compared with the analytical prediction. A comparison shows that the analytical description is accurate and since it only requires numerical data that are computationally more efficient to acquire than performing the rigorous nonlinear simulation, it can serve as the main method for future designs for any parametric process involving leaky Bloch modes.

The paper is structured as follows. Section II is dedicated to a rigorous theoretical formulation of the SHG process in a PCSW involving leaky SH modes. In Sec. III we present a design for phase matching a lossless slow-light mode at the FH frequency to a leaky mode at the SH frequency in a $LiNbO_3$ PCSW and the SH power is calculated using the analytical formulas. Section IV presents the result of the nonlinear FDTD simulation for this design and its comparison with the analytical prediction. Section V includes a summary and a discussion regarding further implications of the results. In the Appendix we present some details of our numerical calculations.

II. THEORY

In this section we analytically describe phase-matched SHG in PCSWs between a lossless FH mode and leaky SH modes. Although we target slow-light modes, we make no specific assumption regarding the magnitude of the group velocities of the modes involved. Therefore, our analysis can be used for any periodic structure with slow or fast modes. For a nonlinear process involving only lossless Bloch modes, one can use the coupled-mode theory based on the conjugated Lorentz reciprocity theorem [10,13]. However, a lossy mode no longer exhibits orthogonality with its conjugate, preventing us from using the conjugated reciprocity theorem. A lossy mode is biorthogonal to a set of modes called the adjoint modes [25–27]. The Lorentz reciprocity theorem has already been reformulated using these adjoint modes to develop a nonlinear coupled-mode theory for lossy periodic structures [18]. For reciprocal materials, the adjoint modes are the same modes of the structure, which means that the adjoint reciprocity theorem for reciprocal materials coincides with the unconjugated reciprocity theorem [12,19,28]. Consequently, the biorthogonality condition will simplify to an unconjugated orthogonality relation between the Bloch modes of the structure [19], which only gives a nonzero value when a mode is mixed with its backward-propagating counterpart. For our reciprocal structure, we use the adjoint formalism and adapt it to the case of phase-matched SHG involving lossy Bloch modes, where the adjoint of a lossy mode is its backward-propagating counterpart.

We used the general term lossy instead of leaky, as the type of loss in the adjoint formalism is not restricted to the leakage loss and could also include material absorption when needed. However, leaky modes offer an extra subtlety. Although the leaky mode of a waveguide is mainly concentrated in the waveguide region, it has an almost exponentially rising radiation tail in the direction transverse to the waveguide [12]. In evaluating integrals over infinite dimensions involving leaky modes, one has to be aware of this rising tail. Such integrals usually appear in the form of overlap integrals in the efficiency of the SHG process. This problem especially has attracted much attention in recent years in the field of nano-optics in studying the dynamics of open nanoresonators and cavities [29–33]. Quasinormal modes (QNMs), introduced by Leung *et al.* [34], are used as the basis for modal expansion in open resonators, where eigenmodes have complex frequencies as the eigenvalue, are mainly concentrated in and around the resonator area, and have rising radiation tails away from the

resonator. This formalism was extended to periodic guiding structures [19], introducing QNBMs as the eigenmodes of the system with complex wave vectors, which solves both the theoretical and numerical problems of using leaky modes for modal expansion. In the work by Lecamp *et al.* [19], QNBMs refer to all the eigenmodes of a periodic structure that are surrounded by a specific choice of the perfectly-matched-layer (PML) boundary condition. These eigenmodes can be classified based on how the specific choice of PML properties affects them. One category consists of the continuum of the radiation modes that is discretized in the presence of PMLs. These modes strongly depend on the PML properties. The other category is the modes that are not sensitive to the choice of PML and can be thought of as the true modes of the waveguide structure. These modes can be bound or leaky with a small imaginary part of the complex wave vector. In our work we use the term QNBM to refer only to this second category of modes. This is analogous to the QNM of a cavity, where the QNM with a complex frequency is a leaky mode that is mainly concentrated in the cavity region and the QNBM with a complex wave vector is a leaky mode that is concentrated in the waveguide region.

We start by defining the QNBMs at the FH and SH frequencies in the complex representation

$$\{\boldsymbol{E}_F,\boldsymbol{H}_F\}(\boldsymbol{r}) = \{\boldsymbol{e}_F,\boldsymbol{h}_F\}(\boldsymbol{r})e^{ik_F x}, \tag{1a}$$

$$\{\boldsymbol{E}_{S_n},\boldsymbol{H}_{S_n}\}(\boldsymbol{r}) = \{\boldsymbol{e}_{S_n},\boldsymbol{h}_{S_n}\}(\boldsymbol{r})e^{ik_{S_n}x-\alpha_n x}, \tag{1b}$$

whereby

$$\{\boldsymbol{e}_{F,S_n},\boldsymbol{h}_{F,S_n}\}(\boldsymbol{r}) = \{\boldsymbol{e}_{F,S_n},\boldsymbol{h}_{F,S_n}\}(\boldsymbol{r}+a\hat{\boldsymbol{x}}). \tag{2}$$

The indices F and S correspond to the time-harmonic fields (time dependence of $e^{-i\omega t}$) at the FH frequency ω_F and the SH frequency ω_S. A single mode is assumed for the FH and the index n runs over the QNBMs present at the SH frequency. Further, $\boldsymbol{E}(\boldsymbol{r})$ is the electric field, $\boldsymbol{H}(\boldsymbol{r})$ is the magnetic field, and $\boldsymbol{e}(\boldsymbol{r})$ and $\boldsymbol{h}(\boldsymbol{r})$ are their corresponding Bloch mode profiles. The propagation direction is x, as shown in Fig. 1. Here $\boldsymbol{r}$ is the position vector, a is the lattice constant or period, $\hat{\boldsymbol{x}}$ is the unit vector in the x direction, and k is the wave number in the propagation direction. For the lossy SH modes, we express the complex wave numbers as $k = k_S + i\alpha$, where $1/\alpha$ is the decay length of the SH mode. The electric and magnetic fields of the unperturbed system are related by the source-free Maxwell's equations

$$\nabla \times \boldsymbol{E}_{F,S_n} = i\omega_{F,S}\mu_0 \boldsymbol{H}_{F,S_n}, \tag{3a}$$

$$\nabla \times \boldsymbol{H}_{F,S_n} = -i\omega_{F,S}\epsilon_0\bar{\epsilon}_{F,S}\boldsymbol{E}_{F,S_n}. \tag{3b}$$

Here $\bar{\epsilon}_{F,S}(\boldsymbol{r}) = \bar{\epsilon}_{F,S}(\boldsymbol{r}+a\hat{\boldsymbol{x}})$ are the relative permittivity tensors of the structure at FH and SH frequencies. This is a symmetric tensor that could be complex valued, meaning that the material is reciprocal but could be anisotropic and lossy.

In the perturbed case, the perturbation is caused by the nonlinearity. The undepleted pump approximation (UPA) is assumed for the FH mode, which is a reasonable approximation for experimentally realizable situations. The UPA requires the amplitude of the FH mode to stay the same as in the unperturbed case in Eq. (1a). The perturbed SH field consists of all the QNBMs present at the SH frequency, each with an amplitude $A_{S_n}(x)$ to be found:

$$\{\boldsymbol{E}'_S,\boldsymbol{H}'_S\}(\boldsymbol{r}) \approx \sum_n A_{S_n}(x)\{\boldsymbol{E}_{S_n},\boldsymbol{H}_{S_n}\}(\boldsymbol{r}). \tag{4}$$

Equation (4) is an approximation. To be exact, in addition to the sum over the QNBMs, the right-hand side of Eq. (4) should also include an integral over the continuum of the radiation modes. In the case of a PCSW, where the FH pump is concentrated around the waveguide region and we are only interested in the generated SH around this waveguide region, Eq. (4) is a good approximation. We make this approximation following that made for QNMs of a resonant structure [29,30], where the QNM expansion without the radiation modes is a good approximation for describing the light dynamics in regions inside and close to the resonator.

The perturbed Maxwell's equations for the SH frequency include the nonlinear polarization $\boldsymbol{P}_{\rm nl}$:

$$\nabla \times \boldsymbol{E}'_S = i\omega_S\mu_0\boldsymbol{H}'_S, \tag{5a}$$

$$\nabla \times \boldsymbol{H}'_S = -i\omega_S\epsilon_0\bar{\epsilon}_S\boldsymbol{E}'_S - i\omega_S\boldsymbol{P}_{\rm nl}, \tag{5b}$$

where $\boldsymbol{P}_{\rm nl}$ for a SHG process can be formulated using contracted notation [35]

$$\boldsymbol{P}_{\rm nl} = 2\epsilon_0 e^{i2k_F x}\boldsymbol{p}_{\rm nl} = 2\epsilon_0 e^{i2k_F x}\bar{d}(\boldsymbol{r})\begin{bmatrix} e_{x_F}^2 \\ e_{y_F}^2 \\ e_{z_F}^2 \\ 2e_{y_F}e_{z_F} \\ 2e_{x_F}e_{z_F} \\ 2e_{x_F}e_{y_F}\end{bmatrix}. \tag{6}$$

Here $\bar{d}(\boldsymbol{r}) = \bar{d}(\boldsymbol{r}+a\hat{\boldsymbol{x}})$ is the nonlinear susceptibility tensor of the material and has to be arranged in a way that the choice of crystallographic basis matches the choice of the coordinate axis. We use the periodicity of Bloch modes to introduce the periodic variable $\boldsymbol{p}_{\rm nl}(\boldsymbol{r}) = \boldsymbol{p}_{\rm nl}(\boldsymbol{r}+a\hat{\boldsymbol{x}})$. To find $A_{S_n}(x)$ for each QNBM, we use the adjoint reciprocity theorem [18]

$$\nabla\cdot\left(\boldsymbol{E}^\dagger_{S_n}\times\boldsymbol{H}'_S - \boldsymbol{E}'_S\times\boldsymbol{H}^\dagger_{S_n}\right) = i\omega_S\boldsymbol{P}_{\rm NL}\cdot\boldsymbol{E}^\dagger_{S_n}, \tag{7}$$

where the adjoint to each QNBM mode is its backward-propagating counterpart

$$\{\boldsymbol{E}^\dagger_{S_n},\boldsymbol{H}^\dagger_{S_n}\}(\boldsymbol{r}) = \{\boldsymbol{e}^\dagger_{S_n},\boldsymbol{h}^\dagger_{S_n}\}(\boldsymbol{r})e^{-ik_{S_n}x+\alpha_n x}. \tag{8}$$

If the structure possesses a mirror symmetry with respect to the propagation direction, the Bloch mode profile of the forward- and backward-propagating modes can be connected to each other [18]. In the specific case of the PCSW shown in Fig. 1, the supercell of the structure is inversion symmetric with respect to the point at the center of the supercell, which simplifies the relation for deriving the adjoint mode profiles to $\boldsymbol{e}^\dagger_S(\boldsymbol{r}) = -\boldsymbol{e}_S(-\boldsymbol{r})$ and $\boldsymbol{h}^\dagger_S(\boldsymbol{r}) = \boldsymbol{h}_S(-\boldsymbol{r})$ [27]. The biorthogonality relation between QNBMs and their adjoints is [19]

$$\iint_{-\infty}^{+\infty}\left(\boldsymbol{e}^\dagger_{S_m}\times\boldsymbol{h}_{S_n} - \boldsymbol{e}_{S_n}\times\boldsymbol{h}^\dagger_{S_m}\right)\cdot\boldsymbol{x}\,dy\,dz = \delta_{nm}\mathcal{F}_n, \tag{9}$$

where $\mathcal{F}_n$ is referred to as the adjoint flux [27] and is a finite x-independent quantity.

To find $A_{S_n}(x)$ from Eq. (7), we take the volume integral of both sides of Eq. (7) over a supercell and use the divergence

theorem on the left-hand side, which turns the volume integral into a surface integral over the supercell. We use a supercell volume because it allows us to find a closed-form expression for A using the periodicity of the modes. Together, by using Eqs. (1b), (4), (6), and (8) with Eq. (7) we get

$$\sum_m \oint_S A_{S_m}(x)\left(\boldsymbol{e}^{\dagger}_{S_n} \times \boldsymbol{h}_{S_m} - \boldsymbol{e}_{S_m} \times \boldsymbol{h}^{\dagger}_{S_n}\right) \cdot d\boldsymbol{S} = i2\omega_S \epsilon_0 \int_\Omega \exp(2ik_F x - ik_{S_n} x + \alpha x)\boldsymbol{p}_{\mathrm{nl}} \cdot \boldsymbol{e}^{\dagger}_{S_n} dV, \quad (10)$$

where Ω is the volume of one supercell, shown in Fig. 1, and S is the closed surface surrounding it. When the guiding structure is surrounded by an outgoing boundary condition, the four surfaces closing the supercell in the transverse directions will not contribute to the surface integral on the left-hand side of Eq. (10) [19]. As a result, the closed surface integral will turn into two surface integrals over the cross sections of the supercell that are perpendicular to the propagation direction, for which we use the biorthogonality relation of Eq. (9). This simplifies Eq. (10) to

$$A_{S_n}(x+a) - A_{S_n}(x) = \frac{i2\omega_S\epsilon_0}{\mathcal{F}_n} \int_\Omega \exp(2ik_F x - ik_{S_n} x + \alpha x) \times \boldsymbol{p}_{\mathrm{nl}} \cdot \boldsymbol{e}^{\dagger}_{S_n} dV. \quad (11)$$

This equation gives the change in $A_{S_n}(x)$ over the length of a. In principle, $A_{S_n}(x = x_1)$ can be calculated for any value of x_1, given that we have its initial value at some other point, e.g., $A_{S_n}(x_0)$. Then we only need to take the integral on the right-hand side of Eq. (11) over a volume starting from x_0 and ending at x_1.

To find a closed-form expression for A, we make the slowly varying envelope approximation (SVEA) for a periodic structure [10]. In this case, the SVEA is only valid when the SH mode has a wave number close to the phase-matching condition and a decay length $L^{\mathrm{decay}} \equiv 1/\alpha$ much longer than a period. We assume that only one SH mode satisfies the phase-matching condition, which is a reasonable assumption for the SHG application. Hence, we drop the index n for the rest of the calculation. The phase-matching condition for a periodic structure is [36]

$$\Delta k = k_S - 2k_F - \frac{2\pi\,\Delta q}{a} = 0, \quad \Delta q = 0,1,2,\ldots. \quad (12)$$

If the system is close to this condition such that $\Delta k \ll 1/a$, then $\exp(-i\,\Delta k x)$ can be approximated as a constant function over the length of a supercell and can be pulled out of the volume integral on the right-hand side of Eq. (11). Moreover, if the decay length of the SH mode is much longer than one period, $\exp(+\alpha x)$ can also be pulled out of the integral. The remaining functions present in the volume integral are periodic. Now we can make the SVEA $A_S(X+a) - A_S(X) \approx a\partial A_S/\partial X$, where X is a discrete coordinate referring to the start of every supercell. Consequently, Eq. (11) results in

$$\frac{\partial A_S}{\partial X} = \frac{i2\omega_S\epsilon_0}{a} e^{(-i\Delta k+\alpha)X} \frac{\mathcal{V}}{\mathcal{F}}, \quad (13)$$

where

$$\mathcal{V} \equiv \int_\Omega \exp\left(-i\frac{2\pi\,\Delta q}{a}x\right)\boldsymbol{p}_{\mathrm{nl}} \cdot \boldsymbol{e}^{\dagger}_S dV \quad (14)$$

is the overlap integral and determines the efficiency of the SHG process. Equation (13) is a first-order differential equation and can be solved using the initial condition $A_S(X=0) = 0$:

$$A_S(X) = \frac{i2\omega_S\epsilon_0}{a} \frac{e^{(-i\Delta k+\alpha)X} - 1}{-i\Delta k + \alpha} \frac{\mathcal{V}}{\mathcal{F}}. \quad (15)$$

With A at hand, we can find the generated SH power as a function of the input FH power. The starting point is to integrate the component of the Poynting vector in the propagation direction over the yz plane for both modes:

$$\mathcal{P}_{\mathcal{F}} = \frac{1}{2}\iint_{-\infty}^{+\infty} \mathrm{Re}[\boldsymbol{e}_F \times \boldsymbol{h}^*_F] \cdot \hat{\boldsymbol{x}}\, dy\, dz, \quad (16)$$

$$\mathcal{P}_S(X) = \frac{|e^{-\alpha X} A_S(X)|^2}{2} \int_{-H/2}^{+H/2}\int_{-W/2}^{+W/2} \times \mathrm{Re}[\boldsymbol{e}_S \times \boldsymbol{h}^*_S] \cdot \hat{\boldsymbol{x}}\, dy\, dz. \quad (17)$$

Here W and H specify the width and height of an arbitrary rectangle around the waveguide, defined to avoid the infinite value of the Poynting vector integral of the leaky QNBM. As stated by Snyder and Love [12], the power of a leaky mode is rather an intuitive concept for understanding leaky modes. In our case, this is not as arbitrary of a choice because we have to choose W and H in a way to correspond to regions close to the waveguide, where the QNBM expansion is valid. Moreover, the assumption that only one SH mode is phase matched and is dominantly contributing to the SHG process has a theoretical convenience in determining the total SH power in Eq. (17). Because modes of a leaky system are not power orthogonal to each other, the total power in general can no longer be presented as the sum of the powers in each mode, but should include some cross terms between the modes [37]. The single-mode approximation avoids this complication. We discuss the effect of this approximation when comparing our analytical result with the rigorous nonlinear simulation.

To normalize the calculated power and make it independent of the absolute value of the Bloch mode profiles, we insert the group velocities of the modes into Eq. (17). As a result, one can utilize the field profiles of Bloch modes found from any numerical method in the analytical calculations. For a lossy Bloch mode, the group velocity is no longer equal to the energy velocity and simply is a relation that connects the complex-valued derivative $d\omega/dk$ to the field profiles of the mode [27]. This relation for the complex group velocity of the SH mode is [19,27]

$$v_{gs} = \frac{c}{n_{gs}} = \frac{a\iint_{-\infty}^{+\infty}(\boldsymbol{e}^{\dagger}_S \times \boldsymbol{h}_S - \boldsymbol{e}_S \times \boldsymbol{h}^{\dagger}_S)\cdot \boldsymbol{x}\, dy\, dz}{2\int_\Omega \boldsymbol{d}_S \cdot \boldsymbol{e}^{\dagger}_S dV}, \quad (18)$$

where n_g is the complex group index and $\boldsymbol{d} = \epsilon_0\bar{\epsilon}\boldsymbol{e}$ is the displacement field profile of the Bloch mode. For a lossless FH mode, the adjoint fields can be related to the conjugated fields through $\boldsymbol{e}^{\dagger}_F(\boldsymbol{r}) = \boldsymbol{e}^*_F(\boldsymbol{r})$ and $\boldsymbol{h}^{\dagger}_F(\boldsymbol{r}) = -\boldsymbol{h}^*_F(\boldsymbol{r})$ [19,27]. Using these relations, Eq. (18) can be simplified to the real-valued

group-velocity relation for a lossless Bloch mode [36]:

$$v_{g_F} = \frac{c}{n_{g_F}} = \frac{2a\mathcal{P}_F}{\int_\Omega \boldsymbol{d}_F \cdot \boldsymbol{e}_F^* dV}. \tag{19}$$

It should be noted that both Eqs. (18) and (19) neglect the dispersion in the material permittivity around each of the FH and SH frequencies. This is a justified approximation in periodic structures made of transparent dielectric materials, where the modal dispersion induced by the structuring is far stronger than the material dispersion. However, in plasmonic structures the material dispersion must be included [29,30]. The exact relation for the group velocity including material dispersion can be found in Ref. [27].

Finally, using Eq. (16)–(19) in combination with Eq. (15), after some rearrangement we get

$$\mathcal{P}_S(X) = \frac{\mathcal{P}_F^2}{\mathcal{P}_{\text{eff}}} \mathcal{R} n_{g_F}^2 |n_{g_S}| \left| \frac{e^{-\alpha X} - e^{-i\Delta k X}}{a(-i\Delta k + \alpha)} \right|^2, \tag{20}$$

where we have defined variables $\mathcal{R}$ and $\mathcal{P}_{\text{eff}}$ as follows:

$$\mathcal{R} \equiv \frac{2\int_{-H/2}^{+H/2}\int_{-W/2}^{+W/2} \text{Re}[\boldsymbol{e}_S \times \boldsymbol{h}_S^*] \cdot \boldsymbol{x}\, dy\, dz}{\left|\iint_{-\infty}^{+\infty} (\boldsymbol{e}_S^\dagger \times \boldsymbol{h}_S - \boldsymbol{e}_S \times \boldsymbol{h}_S^\dagger) \cdot \boldsymbol{x}\, dy\, dz\right|}, \tag{21}$$

$$\frac{1}{\mathcal{P}_{\text{eff}}} \equiv \frac{\frac{2\omega_S^2 a^3}{c^3} \left| \int_\Omega e^{-i\frac{2\pi\Delta q}{a}x} \epsilon_0 \boldsymbol{p}_{\text{nl}} \cdot \boldsymbol{e}_S^\dagger dV \right|^2}{\left| \int_\Omega \boldsymbol{d}_S \cdot \boldsymbol{e}_S^\dagger dV \right| \left(\int_\Omega \boldsymbol{d}_F \cdot \boldsymbol{e}_F^* dV \right)^2}. \tag{22}$$

Equations (20)–(22) are the main results of the analytical calculation and represent the power of the generated SH signal. Equation (20) reproduces the general expected effects for SHG in the presence of loss, which is the existence of a saturation length for the generated SH power, equal to the decay length of the SH mode [38]. This means that the generated SH power gradually balances with the radiating SH power, resulting in a constant level of SH power in the waveguide. A different result of this calculation is that it reveals the group index dependence of a parametric process involving lossy modes. For a SHG process in a 2D PC involving only lossless modes, it has been shown that the generated SH power enhances quadratically and linearly with respect to n_{g_F} and n_{g_S}, respectively [13], where both group indices are real numbers. However, when a mode is lossy, it has a complex group index [27] and as derived in Eq. (20) it is the absolute value of this complex group index that affects the efficiency of the process. Equation (21) defines $\mathcal{R}$ as a dimensionless parameter and its value is dependent on the choice of W and H. This factor appears as the result of trying to define a power for the leaky mode. A closer look at $\mathcal{R}$ reveals that it is the power of the SH Bloch mode profile divided by its adjoint flux and it is exactly equal to 1 for a lossless mode with an infinite W and H. Equation (22) defines $\mathcal{P}_{\text{eff}}$ as an effective power. The nominator of Eq. (22) includes the overlap integral between the backward-propagating SH mode and the nonlinear polarization that is generated by the FH mode. To have an efficient nonlinear interaction, this overlap has to be maximized by the proper choice of crystal orientation and the symmetry of the dominant components of the electric field profile of the modes involved. The denominator includes the energy density integral for the FH mode, whereas for the SH mode the integral is no longer the energy density, but rather an adjoint density [27]. These integrals in the denominator serve to normalize $\mathcal{P}_{\text{eff}}$ so that it is independent of the choice of the absolute value of the Bloch mode profiles.

Finally, we investigate the phase-matching part of Eq. (20) in more detail. For this we define the phase-matching function PM as

$$\text{PM}(\omega_F, L) \equiv \left| \frac{e^{-\alpha L} - e^{-i\Delta k(\omega_F)L}}{a[-i\Delta k(\omega_F) + \alpha]} \right|^2, \tag{23}$$

where L is the length of the structure and the phase mismatch Δk is a function of the frequency (or the wavelength) of the input FH pump. In a lossless system, the phase-matching function is of the form $\text{sinc}^2(\Delta k L/2)$ [35], which gets narrower as L is increased. In the presence of loss, for $L \to \infty$, PM approaches a Lorentzian function of the form $1/(\Delta k^2 + \alpha^2)$, independent of L. Consequently, there is a lower limit to the k bandwidth of the phase-matching function, set by the amount of loss: The longer the decay length of the SH mode is, the narrower the k bandwidth of the phase-matching function becomes. However, this bandwidth can get even narrower with respect to ω_F, when $dk/d\omega$ is large in the presence of slow light. This is because when ω_F of the pump is detuned from the phase-matching frequency, Δk grows faster proportional to n_{g_F}. Consequently, with a slow mode involved in a parametric process, narrower frequency bandwidths can be achieved with shorter structures, compared to the cases involving nonslow modes.

To check the validity of the analytical description through comparison with a nonlinear numerical calculation, a specific design is needed. As can be seen, to evaluate the generated SH power through Eqs. (20)–(22), we need to know the linear properties of the Bloch modes involved in the interaction. This includes the Bloch mode profiles, group indices, and the real- or complex-valued wave vectors. In the next section we propose a design, investigate its linear properties that concern the nonlinear interaction, and implement these numerical data in Eqs. (20)–(22) to find $\mathcal{P}_S(X)$.

III. LINEAR SIMULATION

In this section we propose a design for phase-matched SHG in a $LiNbO_3$ PCSW. As was discussed in the previous section, we want the FH mode to be slow for better SHG efficiency and a narrower phase-matching bandwidth. We need to phase match this slow mode to a leaky SH mode to exhibit the phase-matching effects. The process of the design involves only linear simulations to find the properties of the Bloch modes, such as the band diagram and field profiles. By implementing these linear data in Eqs. (20)–(22), we find the generated SH power as a function of the length of the structure.

We have performed all of our FDTD simulations with a resolution of $a/40$, using the freely available software package MEEP [39]. We use two different sets of refractive indices of $LiNbO_3$ [40] in our FDTD simulations. One is for the FH simulations at the wavelength of $\lambda_{\text{FH}} = 1550$ nm with $n_e = 2.1376$ and $n_o = 2.2111$, where indices e and o stand for the extraordinary and ordinary components of refractive index tensor. The other is for the SH simulations at the wavelength of $\lambda_{\text{SH}} = 775$ nm with $n_e = 2.1784$ and $n_o = 2.2587$. For finding the dispersion relation of the modes around each of

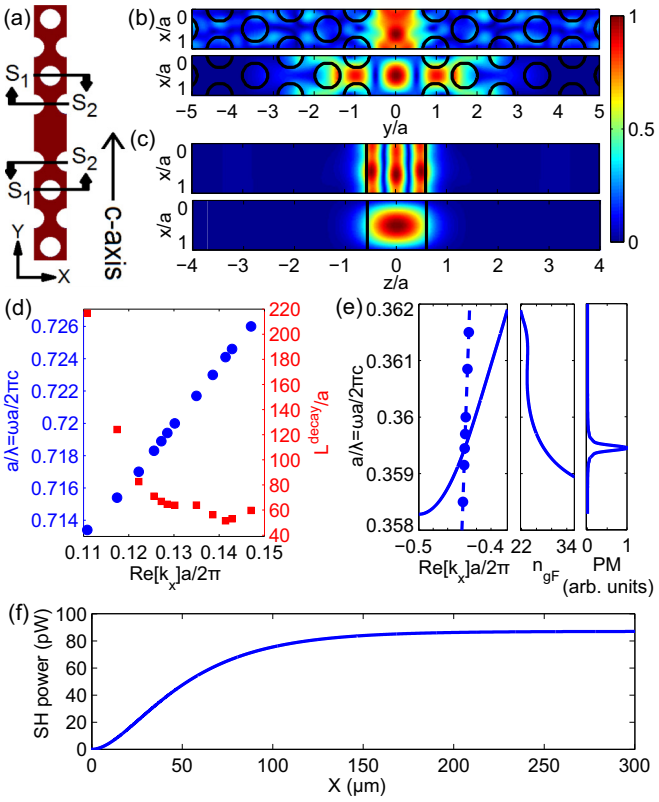

FIG. 2. (Color online) (a) Dispersion engineering design for low dispersion slow light, where the first and second rows of holes are shifted outward and inward, respectively. The c axis of the $LiNbO_3$ crystal is along the y direction. (b) and (c) Absolute value of the E_y field component for the TE_{02} SH field (top) and of the slow FH mode (bottom) at (b) the $z = 0$ plane and (c) the $y = 0$ plane. (d) Band diagram of the TE_{02} mode around the SH frequency. The blue closed circles (left axis) are the normalized frequencies and the red closed squares (right axis) are the decay lengths. (e) On the left the solid line is the band diagram of the slow-light mode. The closed circles (with a dashed line passing through it) are the band of the SH mode translated using the phase-matching condition. Shown in the middle is the group index of the FH slow mode. On the right is the phase-matching function. (f) Generated SH power $\mathcal{P}_S(X)$ along the PCSW using Eqs. (20)–(22), assuming an input FH power of 1 mW.

these wavelengths, we neglect the dispersion of the material in our FDTD simulations. For a monochromatic excitation of the FH wave at $\lambda_{FH} = 1550$ nm the phase matching is still exact. The only quantities that will be slightly affected through this approximation, as was discussed after Eqs. (18) and (19), are the group velocities of the modes that are derived from each of the calculated band diagrams.

The final design is shown in Fig. 2(a). We use a hexagonal lattice to create a frequency band gap for the TE-like (z-even [1]) FH mode. A waveguide is created by removing a row of holes. We choose the crystal to have its c axis (extraordinary axis) along the y direction. This choice is made to make use of the strongest component of the nonlinearity tensor d_{33} that most efficiently mediates the nonlinear interaction between TE-like modes, which have their dominant electric field in the y direction. We engineer the FH mode to achieve a low-dispersion slow-light mode, i.e., in a certain range of frequencies the group index of the mode is nearly constant. This reduces the sensitivity of the group index of the FH mode at the point of phase matching with respect to the frequency shifts of the band that could be caused by inaccuracy in a possible fabrication. Low-dispersion slow light in PCSWs can be achieved by altering the geometry of the structure near the waveguiding region and different approaches for such dispersion engineering exist [41–44]. In our design we use transversal shifting of the first and second rows of holes adjacent to the waveguide [42], as shown in Fig. 2(a). We choose this method as it seems most feasible to realize in a potential fabrication of the device. The parameters of the structure are as follows: the radius of holes $R/a = 0.3$, the thickness of the slab $h/a = 1.2$, and the transversal shifts of rows $S_1/a = 0.1$ and $S_2/a = 0.05$.

The choice for the FH mode is dictated by the availability of a lossless slow-light mode that is susceptible to dispersion engineering. This is the mode with a z-even–y-odd symmetry and a dominant electric-field component E_y that looks even across the $z = 0$ and $y = 0$ planes. For getting the highest overlap integral for the nonlinear process, we choose a SH mode of the same symmetry. The absolute value of the E_y component for both modes is shown in Figs. 2(b) and 2(c) in a supercell. As far as the waveguide region is concerned, we can approximately think of the FH and the SH modes as a TE_{00} and a TE_{02} mode, respectively. The reason for choosing this particular leaky SH mode is as follows. First, it has no nodes in its dominant field profile in the y direction, giving it a confined field profile and hence low interactions with the adjacent rows of holes. This eventually results in low leakage losses. Second, it has two nodes in its dominant field profile in the z direction, making it more sensitive than the FH mode to a change of the thickness of the slab. This property of the mode is of main importance for reaching and tuning the modal phase matching. By increasing (decreasing) the thickness of the slab, the frequency of the SH band shifts down (up) in the band diagram with respect to the frequency of the FH band. We have used this tuning property in the design process to reach modal phase matching at a point where the SH mode has a low loss and the FH mode has a low group velocity.

The band diagram for the SH mode is shown in Fig. 2(d), along with its decay length. The decay length of a mode is defined as the inverse of the imaginary part of its wave number $L^{\text{decay}} \equiv 1/\alpha$. Both the decay length and the real-valued frequency are plotted as a function of the real part of the wave number. We have found the band in the region $0.11 < \text{Re}[k_x]a/2\pi < 0.15$, which is around the phase-matching condition. In Fig. 2(e) the slow FH band is shown along with its corresponding group index. The band of the slow mode is shown in the negative part of the first Brillouin zone (BZ), as the forward-propagating slow mode has a negative k-value in the first BZ. This can also be seen from the positive slope of the band diagram, which indicates a positive group velocity and forward propagation in the x direction. The region of low group index variation can be seen around $n_{g_F} \approx 24$. The dashed line in the left figure of Fig. 2(e), passing through the closed circles, represents the SH band, translated according to the phase-matching condition. For this translation, the frequency of each point in the SH band is divided by 2 and its k vector is translated using

$(\frac{k_S a}{2\pi} - 1)/2$, following Eq. (12) with $\Delta q = 1$. The crossing is at $\frac{k_F a}{2\pi} = -0.4364$ and $\frac{\omega_F a}{2\pi c} = 0.359\,44$ for FH, which corresponds to $\frac{k_S a}{2\pi} = 0.1272$ and $\frac{\omega_S a}{2\pi c} = 0.718\,89$ for SH. At the phase-matching point, the group indices can be found from the band diagram and are $n_{g_F} = 28$ and $n_{g_S} = 2.67 + i\,1.26$. The decay length of the SH mode at the point of phase matching is about 67 periods. At the end of the design, we set the lattice constant to $a = 0.557\ \mu$m, which fixes the FH wavelength at $\lambda_{\mathrm{FH}} = 1550$ nm.

To find the generated SH power, we need to evaluate $\mathcal{R}$ and $\mathcal{P}_{\mathrm{eff}}$ from Eqs. (21) and (22). For this we use the Bloch mode profile of both modes, such as the ones shown in Figs. 2(b) and 2(c) (along with the other components of the field). However, with the rising radiation tail of leaky modes, it is not obvious that the integrals in the denominators of Eqs. (21) and (22) result in a finite value. The finiteness of such integrals was mathematically proven for specific geometries [34,45] by performing a complex-coordinate transformation that causes the exponential tails of the leaky mode to decay, but preserves the total value of the integral. This was later generalized [19,29] through the use of the PML boundary condition, which acts as a numerical equivalent of a complex-coordinate transformation for any structure with an outgoing boundary condition. In this way, the fields inside the PMLs can be used for the integration and because the fields in this region go to zero, the integrals are convergent. We use this property of the PMLs for correct evaluation of our integrals. The details of the numerical procedure are outlined in the Appendix. Moreover, for finding the generated SH power in physical units, we need to fix some variables. We set $W = H = 2a$, which is not a strict choice, but it is important to keep it consistent for the power calculation in the next section using the rigorous nonlinear calculation so that they are comparable. We choose the forward-propagating power in the FH mode to be 1 mW. We only consider the d_{33} coefficient of the d tensor in the calculation, as it later on simplifies our rigorous nonlinear simulation. It is also a good approximation if the $LiNbO_3$ crystal has its extraordinary axis in the y direction and both FH and SH modes are TE-like. We set $d_{33} = -20.6$ pm/V [46].

With these at hand, we have all the numerical data to evaluate Eqs. (20)–(22). The calculated $\mathcal{P}_S(X)$ for this particular design is shown in Fig. 2(f). We see the quadratic rise of power at the beginning of the structure, which saturates for propagation lengths greater than 120 μm. This is the signature of a SHG process with a lossy SH mode. This also means that structure lengths more than about 120 μm are not of much benefit for enhanced efficiency. At this length, the generated SH is about 80 pW. This limits the total efficiency of this specific design to about 8×10^{-5} W^{-1}. Furthermore, we can calculate the phase-matching function of Eq. (23) using the band diagram of the modes and this structure length to show the narrow-band property in the presence of slow light. This is shown in Fig. 2(e). In physical units, this results in a bandwidth of less than 1 nm. This narrow bandwidth for such a short structure is caused by the large angle between the crossing of the band diagram of the FH and the SH modes in Fig. 2(e) and illustrates the benefit of slow light in achieving narrow-band interactions. To test the validity of the analytical model, in the next section we perform a rigorous nonlinear FDTD simulation and compare the results for the generated SH power.

IV. NONLINEAR SIMULATION

In this section we perform a rigorous nonlinear FDTD simulation in the UPA for the design of the previous section to approve the validity of the analytical prediction. The FH field induces the nonlinear polarization, which acts as a source to excite the SH mode, as is evident from Eq. (5b). In the UPA this source term does not change along the propagation direction. We generate this source of nonlinear polarization by using the Bloch mode profile of the FH mode and by reproducing a purely-forward-propagating slow mode in a structure with a length of 235 periods. This corresponds to 131 μm, which, as seen before, is long enough to exhibit the saturation effect. Afterward, we extract the complex-valued E_y component of the FH field, square it, and multiply it by the spatial function that represents the nonlinearity profile. This gives us $\boldsymbol{P}_{\mathrm{nl}}$ of Eq. (5b), given the reasonable approximation that only the d_{33} component of the nonlinearity tensor is taking part in SHG, which is the same approximation we made for the analytical prediction shown in Fig. 2(f). The SHG simulation is then performed by using this $\boldsymbol{P}_{\mathrm{nl}}$ as a complex-valued source in the same geometry to run the FDTD simulation at the SH frequency. The results of this simulation are shown in Fig. 3. In Fig. 3(a) the absolute value of the E_y component of the generated SH field can be seen around the region where the spatial nonlinear source ends. For finding the generated SH power, we use Eq. (17) with the same $W = H = 2a$ that we used in the previous section. The result for the generated SH power is shown in Fig. 3(b), where the analytical prediction of Fig. 2(f) is also included.

We first investigate the field profile of the generated SH, shown in Fig. 3(a). We see that the generated field resembles that of the TE_{02} mode in Fig. 2, but only in the waveguide region, which is the region over which the QNBM

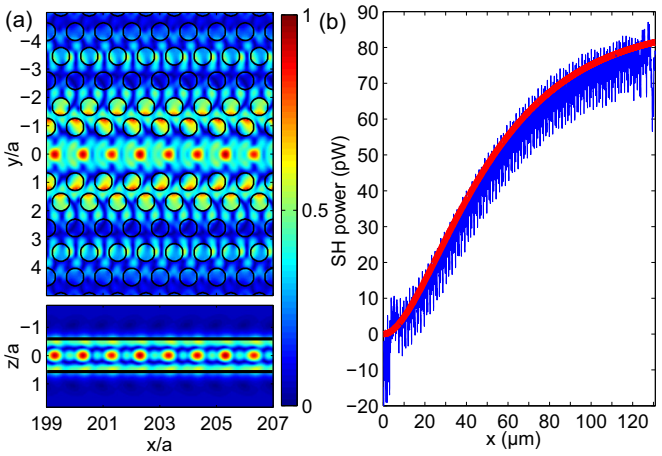

FIG. 3. (Color online) (a) Absolute value of the E_y component of the generated SH field at the end region of the structure at the $z = 0$ (top) and $y = 0$ (bottom) planes. (b) Generated SH power $\mathcal{P}_S(X)$ along the PCSW using the nonlinear FDTD (blue curve) and the analytical prediction (red curve), assuming an input FH power of 1 mW.

is a good approximation for modal expansion. Outside the waveguide region, especially around the first and second rows of holes adjacent to the waveguide, we see a strong field that corresponds to the part of the nonlinear polarization that is not concentrated in the waveguide and overlaps best with the radiation modes of the PC slab, which are not of interest for guided and phase-matched SHG. The main comparison is between the generated SH powers in Fig. 3(b). Overall, the analytical result agrees well with that of the nonlinear FDTD simulation. A distortion in the power can be observed for the nonlinear FDTD at the beginning and the end of the simulation domain, caused by the abrupt starting and ending of the source of nonlinear polarization. Furthermore, the generated power in the nonlinear simulation has an additional oscillation of about ± 8 pW, whereas the analytical result is a smooth curve. This extra oscillation is caused by the out-of-phase generation of the SH power in the other QNBMs present at the SH frequency, including forward- and backward-propagating ones. This is why the generated SH field profile in the line defect is not exactly the same as the field profile of the QNBM shown in Fig. 2, but only resembles that mode profile, as the TE_{02} is the dominant mode contributing to the SHG process. In this case, out of all the out-of-phase SH modes, the ones with the largest overlap integral with the nonlinear polarization are the forward- and backward-propagating TE_{00} modes, contributing dominantly to this power oscillation. Although the analytical formulation can include multiple modes for the SH frequency, we have written the final power assuming only one dominant SH mode. We see from the comparison that this is a good approximation and the phase-matched TE_{02} mode indeed has the dominant role over the other out-of-phase generated modes. Finally, our initial SVEA that was made to get a closed-form differential equation only predicts the amplitude of the generated SH at the beginning of each supercell. This means that the final theoretical formula only describes SHG at the beginning of each supercell. As a result, the theory with the SVEA predicts a smooth monotonic transition of the generated SH power from one supercell to the next. The exact case without the SVEA will still show this monotonic power transition, but additionally some periodic dynamic within the supercell.

V. CONCLUSION

We have analytically described SHG involving lossy Bloch modes in photonic crystal waveguides. The theory was rigorously formulated using an adjoint formalism and quasinormal Bloch modes as the basis for the modal expansion to take into account the loss of the leaky SH modes. We presented a design for phase-matched and guided SHG in a photonic crystal slab waveguide made of lithium niobate, where the FH mode is operating in a slow-light regime. Using this design, we have found good agreement between the result of a rigorous nonlinear FDTD simulation and the prediction of our analytical calculation. The analytical description only requires calculation of the band diagram and the Bloch mode profiles, which needs much less computational resources and can be performed with a much higher resolution, compared to the rigorous nonlinear FDTD simulation. This makes the analytical approach a more efficient method for calculating the SHG efficiency. It is important to note that, although we do our numerical investigation for a specific design and nonlinear process, the theory and numerical methods are equally applicable for any other periodic structures designed for a phase-matched nonlinear process involving lossy Bloch modes.

Having an analytical understanding along with structure designs for phase-matched parametric processes is especially of importance for narrow-band interactions that require control over the spectrum of the generated harmonics. An example is the spontaneous parametric down-conversion (SPDC), in which the second-harmonic mode acts as the pump for the process and a phase-matched interaction is required to control the generation of photon pairs with certain spectral properties [47]. The SHG study in this work is a first step towards the study of photon-pair generation through SPDC in photonic crystal slab waveguides, where dispersion engineering of the slow-light mode can provide possibilities in manipulating the two-photon wave function.

It should be mentioned that, although the quadratic enhancement of the SH power with respect to n_{g_F} is the main reason to use slow light for the FH mode, in a realistic situation, the group index of a mode cannot be increased indefinitely. This is due to the unavoidable presence of loss caused by material absorption and fabrication disorder, which no matter how small will prevent the group velocity of the modes from reaching absolute zero [48,49]. Moreover, such losses themselves are enhanced in the presence of slow light [50]. This means that there should exist an optimum value for the group index of the FH mode to maximize the generated SH power, which could be found, based on the specific amount of loss [51,52], using our analytical formalism.

ACKNOWLEDGMENTS

We wish to acknowledge the financial support from the Carl Zeiss Foundation and the German Research Foundation (SPP1391 Ultrafast Nanooptics).

APPENDIX: DETAILS OF THE NUMERICAL METHODS

Since we are dealing with a leaky mode at the SH frequency, for the numerical simulations it is essential to use the PML boundary condition on the transverse surfaces of the simulation domain to absorb the radiation fields. Correct use of the PMLs also allows the normalization of the leaky modes, as explained before. However, it is known that PMLs do not work properly when a periodic structure is entering them [53]. Consequently, instead of using an infinite number of rows in the transverse direction that makes the rows of holes enter the PMLs, we use a finite number of eight rows in the transverse direction. The finite number of rows is also the case in any realistic experimental scheme. In our case, eight rows of holes is more than enough to confine the FH mode in the transverse direction through the PC band-gap effect. After these eight rows, the slab will have no inhomogeneity and PMLs can be safely put around the structure.

Two different methods are used in our linear FDTD calculations. We need to find the band diagram of the leaky modes with a real frequency $\omega = \omega_R$ and a complex wave

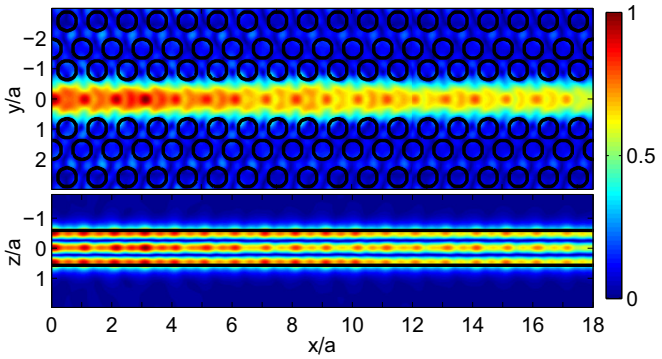

FIG. 4. (Color online) Absolute value of the E_y field component at the $z = 0$ (top) and $y = 0$ (bottom) planes, in a linear FDTD simulation, when the structure is excited from the left side with a cw source at the frequency of $\frac{\omega_S a}{2\pi c} = 0.718\,89$, where the source profile is chosen so that the leaky TE_{02} is dominantly excited.

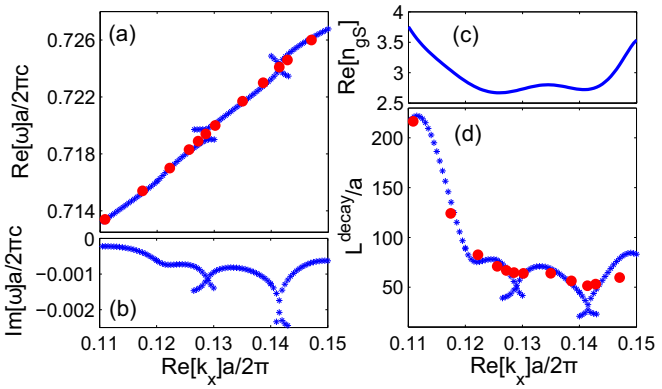

FIG. 5. (Color online) (a) Band diagram of the TE_{02} mode around the SH frequency. The blue crosses are the complex-ω band. The red closed circles are the few points found from the complex-k method. (b) Imaginary part of the frequency of the TE_{02} mode from the complex-ω method. (c) $\mathrm{Re}[n_{gS}]$ from the complex-k band. (d) L^{decay} of the TE_{02} mode, found from the complex-k and the complex-ω methods.

vector $k = k_R + ik_I$. To do this with FDTD, the PCSW structure is excited from one end with a continuous-wave (cw) source of frequency ω_R. The excitation profile is chosen such that it dominantly excites the mode of interest. The resulting field looks like the one shown in Fig. 4. Here k_R of the mode excited can then be found by taking a Fourier transform from the field along the propagation direction. To find the decay length of the mode, and hence $k_I = 1/L^{\mathrm{decay}}$, we fit an exponential to the decaying power in the propagation direction. We refer to this method as the complex-k method. This method is used to find the band diagram of the leaky SH mode in Fig. 2(d). For finding the band diagram of the FH mode, we use a computationally more efficient method, which is implemented in MEEP. In this method, a pulse is excited inside a supercell. The supercell has Floquet-Bloch boundary conditions on its boundaries along the propagation direction, set by $k = k_R$. As this method only uses a supercell as the computational domain, it is more efficient than the complex-k method. The pulse excites the modes of interest inside the supercell. The system evolves for some time after the pulse is stopped. The complex-valued frequencies $\omega = \omega_R + i\omega_I$ of the modes evolving in the supercell are then extracted by analyzing the time evolution of the fields. We refer to this method as the complex-ω method. It is important to note that the results of complex-k and complex-ω methods refer to two different physical situations, which only have exactly equivalent results for lossless bound modes [54,55]. This is why we can use the more efficient complex-ω method for finding the band diagram of the FH mode that has real-valued k and ω.

For finding the field profiles of Bloch modes with a real frequency and complex wave vector, frequency domain solvers can be used [56]. With the FDTD, which is a time-domain solver, we can employ fields such as in Fig. 4 and use a Bloch-mode-extraction algorithm [57] to extract the field profile of the complex-k Bloch modes. This, however, will not be numerically efficient, especially if we are trying to find and study the field profile of leaky modes over a large transverse cross section. Instead, we make an approximation and use the complex-ω method. The complex-ω and complex-k methods give exactly the same results for bound and lossless modes and similar results for modes with small losses [55]. We take this to be a good approximation in finding the field profile of our leaky modes of interest since they only have weak losses. To find the ranges where this is a good approximation, we find the band diagram for the leaky TE_{02} using both methods. Results are shown in Fig. 5. The real and imaginary parts of the frequency found from the complex-ω method are shown in Figs. 5(a) and 5(b), respectively. One could, with a good approximation, relate the complex frequency to the decay length, using the real part of the group index through the relation $L^{\mathrm{decay}} = -c/\mathrm{Re}[n_g]\omega_I$, where $\mathrm{Re}[n_g] = cd\,\mathrm{Re}[k]/d\omega$ is found from the complex-k band diagram [55]. Because we have few points for this band, we fit a polynomial to the points, from which we can get the derivative. The result is shown in Fig. 5(c). From this we find the decay length predicted by the complex-ω simulation, shown in Fig. 5(d). We see that the two methods predict a very close band diagram and decay lengths, except for places where the complex-ω band exhibits frequency splitting in the band and the complex-k band shows a smoother band diagram. Consequently, as long as we are not looking for modes at these places in the band, we can use complex-ω simulations as a good approximation instead of the complex-k ones. Another conclusion from this analysis is that one can even use the complex-ω bands as a computationally efficient way of finding the SH band approximately and optimizing the design to reach phase matching. Once the approximate design has been reached, a few complex-k simulations are enough to determine the band accurately around the phase-matching frequency.

To find the field profile with the complex-ω method, a narrow-frequency-bandwidth pulse, around the frequency ω_R, is excited in a supercell with the periodic boundary condition set by k_R. After the pulse ends, enough time is given to the leaky mode to radiate and reach steady state. In the case of a leaky mode, we reach steady state when a field component of the form $\mathrm{Re}[\boldsymbol{u}(\boldsymbol{r})\exp(-i\omega_R t + \omega_I t)]$, where ω_I is a negative number, reaches a steady-state value for the absolute value of

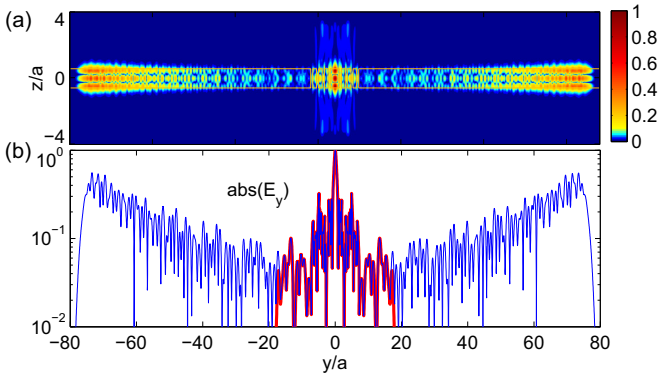

FIG. 6. (Color online) Absolute value of the E_y field component of the SH mode on (a) the $x/a = 0.5$ plane and (b) the $x/a = 0.5, z/a = 0$ line. The color scale in (a) is chosen in a way that the weaker fields are intensified in the plot. In (b) two different supercell dimensions are used.

$\boldsymbol{u}(\boldsymbol{r})$ all over the simulation domain. This means the mode has an amplitude that decays exponentially in time, but the profile of the mode does not change in space. The mode found in this way is the solution of the source-free wave equation in the given geometry. The Bloch field profiles found from this method are shown in Fig. 2.

To see the rising tail of the field for the leaky mode, we perform the simulation in a supercell with a large transverse dimension of $160a$ in the y direction. The result is shown in Fig. 6(a), where the rising tail of the field is clearly visible at the left and right of the simulation domain. To verify that this is a steady-state profile, we find the field profile for the same mode in a supercell with a transverse dimension of $40a$ in the y direction. The absolute value of the field is plotted on a line for the cases of both $40a$ and $160a$ supercells in Fig. 6(b), which shows the exponentially rising tail that looks linear in a logarithmic plot. It also shows that the two field profiles found using two different simulations match exactly over the domain they have in common, verifying that the fields are the steady-state profiles.

Finally, to use the fields inside the PML region for evaluating QNBM field integrals in Eqs. (21) and (22), the main thing to note is that, as long as the integrals have no explicit inclusion of ε and μ, there is no need to know the actual transformation that created the PML. This is the advantage of using the displacement field in Eq. (22). We need to know only the fields, which is the output by MEEP everywhere, including in the PML region. We also do a test to verify that fields in the PML output by MEEP are of physical significance. For this we calculate the complex group index n_{gs} by implementing the fields found from both the $40a$ and $160a$ simulations in Eq. (18) and compare the results. The presence of the large tails of the field in the larger supercell simulation ensures that if a wrong method for handling the fields is used, we will get very different values for n_{gs} in the two cases. However, as a property of the mode, the group index calculated from the fields has to remain unchanged in both cases and also match the value calculated from the complex-ω band diagram. For the $40a$ and $160a$ supercells we find $n_{gs} = 3.1132 + i1.1923$ and $n_{gs} = 3.1134 + i1.1921$, respectively. These values are very close to each other and to that calculated directly from the band diagram, $n_{gs} = 3.1377 + i1.1756$. This test verifies our point.

[1] J. D. Joannopoulos, S. G. Johnson, J. N. Winn, and R. D. Meade, *Photonic Crystals: Molding the Flow of Light*, 2nd ed. (Princeton University Press, Princeton, 2008).

[2] T. F. Krauss, J. Phys. D **40**, 2666 (2007).

[3] M. Soljacic, S. G. Johnson, S. Fan, M. Ibanescu, E. Ippen, and J. D. Joannopoulos, J. Opt. Soc. Am. B **19**, 2052 (2002).

[4] T. Baba, Nat. Photon. **2**, 465 (2008).

[5] K. Rivoire, S. Buckley, F. Hatami, and J. Vučković, Appl. Phys. Lett. **98**, 263113 (2011).

[6] K. Lenglé, L. Bramerie, M. Gay, J. C. Simon, S. Combrié, G. Lehoucq, and A. D. Rossi, Appl. Phys. Lett. **102**, 151114 (2013).

[7] B. Corcoran, C. Monat, C. Grillet, D. J. Moss, B. J. Eggleton, T. P. White, L. O'Faolain, and T. F. Krauss, Nat. Photon. **3**, 206 (2009).

[8] C. Monat, M. Spurny, C. Grillet, L. O'Faolain, T. F. Krauss, B. J. Eggleton, D. Bulla, S. Madden, and B. Luther-Davies, Opt. Lett. **36**, 2818 (2011).

[9] J. Li, L. O'Faolain, and T. F. Krauss, Opt. Express **20**, 17474 (2012).

[10] D. Michaelis, U. Peschel, C. Wächter, and A. Bräuer, Phys. Rev. E **68**, 065601 (2003).

[11] M. Santagiustina, C. G. Someda, G. Vadalà, S. Combrié, and A. D. Rossi, Opt. Express **18**, 21024 (2010).

[12] A. W. Snyder and J. D. Love, *Optical Waveguide Theory* (Chapman and Hall, London, 1983).

[13] R. Iliew, C. Etrich, T. Pertsch, and F. Lederer, Phys. Rev. B **77**, 115124 (2008).

[14] C. Monat, C. Grillet, B. Corcoran, D. J. Moss, B. J. Eggleton, T. P. White, and T. F. Krauss, Opt. Express **18**, 6831 (2010).

[15] C. Nistor, C. Cojocaru, Y. Loiko, J. Trull, and K. Staliunas, J. Opt. A **11**, 114016 (2009).

[16] M. Houe and P. D. Townsend, J. Phys. D **28**, 1747 (1995).

[17] A. S. Helmy, D. C. Hutchings, T. C. Kleckner, J. H. Marsh, A. C. Bryce, J. M. Arnold, C. R. Stanley, J. S. Aitchison, C. T. A. Brown, K. Moutzouris, and M. Ebrahimzadeh, Opt. Lett. **25**, 1370 (2000).

[18] A. A. Sukhorukov, A. S. Solntsev, S. S. Kruk, D. N. Neshev, and Y. S. Kivshar, Opt. Lett. **39**, 462 (2014).

[19] G. Lecamp, J. P. Hugonin, and P. Lalanne, Opt. Express **15**, 11042 (2007).

[20] H. Hartung, E.-B. Kley, T. Gischkat, F. Schrempel, W. Wesch, and A. Tünnermann, Opt. Mater. **33**, 19 (2010).

[21] R. Geiss, S. Diziain, M. Steinert, F. Schrempel, E.-B. Kley, A. Tünnermann, and T. Pertsch, Phys. Status Solidi A **211**, 2421 (2014).
[22] S. Diziain, R. Geiss, M. Zilk, F. Schrempel, E. B. Kley, A. Tünnermann, and T. Pertsch, Appl. Phys. Lett. **103**, 051117 (2013).
[23] R. Geiss, S. Saravi, A. Sergeyev, S. Diziain, F. Setzpfandt, F. Schrempel, R. Grange, E.-B. Kley, A. Tünnermann, and T. Pertsch, Opt. Lett. **40**, 2715 (2015).
[24] A. Sergeyev, R. Geiss, A. S. Solntsev, A. A. Sukhorukov, F. Schrempel, T. Pertsch, and R. Grange, ACS Photon. **2**, 687 (2015).
[25] L. C. Botten, M. S. Craig, R. C. McPhedran, J. L. Adams, and J. R. Andrewartha, Opt. Acta **28**, 1087 (1981).
[26] A. E. Siegman, Opt. Commun. **31**, 369 (1979).
[27] P. Y. Chen, R. C. McPhedran, C. M. de Sterke, C. G. Poulton, A. A. Asatryan, L. C. Botten, and M. J. Steel, Phys. Rev. A **82**, 053825 (2010).
[28] Z. Ruan, G. Veronis, K. L. Vodopyanov, M. M. Fejer, and S. Fan, Opt. Express **17**, 13502 (2009).
[29] C. Sauvan, J. P. Hugonin, I. S. Maksymov, and P. Lalanne, Phys. Rev. Lett. **110**, 237401 (2013).
[30] C. Sauvan, J. P. Hugonin, R. Carminati, and P. Lalanne, Phys. Rev. A **89**, 043825 (2014).
[31] P. T. Kristensen, C. V. Vlack, and S. Hughes, Opt. Lett. **37**, 1649 (2012).
[32] J. R. de Lasson, P. T. Kristensen, J. Mørk, and N. Gregersen, J. Opt. Soc. Am. A **31**, 2142 (2014).
[33] P. T. Kristensen, J. R. de Lasson, and N. Gregersen, Opt. Lett. **39**, 6359 (2014).
[34] P. T. Leung, S. Y. Liu, and K. Young, Phys. Rev. A **49**, 3982 (1994).
[35] R. W. Boyd, *Nonlinear Optics*, 3rd ed. (Academic, New York, 2008).
[36] A. Yariv and P. Yeh, J. Opt. Soc. Am. **67**, 438 (1977).
[37] A. E. Siegman, Proc. SPIE **4436**, 1 (2001).
[38] D. Duchesne, K. A. Rutkowska, M. Volatier, F. Légaré, S. Delprat, M. Chaker, D. Modotto, A. Locatelli, C. De Angelis, M. Sorel, D. N. Christodoulides, G. Salamo, R. Arès, V. Aimez, and R. Morandotti, Opt. Express **19**, 12408 (2011).
[39] A. F. Oskooi, D. Roundy, M. Ibanescu, P. Bermel, J. D. Joannopoulos, and S. G. Johnson, Comput. Phys. Commun. **181**, 687 (2010).
[40] D. E. Zelmon, D. L. Small, and D. Jundt, J. Opt. Soc. Am. B **14**, 3319 (1997).
[41] L. H. Frandsen, A. V. Lavrinenko, J. Fage-Pedersen, and P. I. Borel, Opt. Express **14**, 9444 (2006).
[42] J. Li, T. P. White, L. O'Faolain, A. Gomez-Iglesias, and T. F. Krauss, Opt. Express **16**, 6227 (2008).
[43] J. Liang, L. Y. Ren, M. J. Yun, X. Han, and X. J. Wang, J. Appl. Phys. **110**, 063103 (2011).
[44] F. Wang, J. S. Jensen, and O. Sigmund, Photon. Nanostruct. **10**, 378 (2012).
[45] R. A. Sammut and A. W. Snyder, Appl. Opt. **15**, 1040 (1976).
[46] R. Schiek and T. Pertsch, Opt. Mater. Express **2**, 126 (2012).
[47] W. P. Grice, A. B. U'Ren, and I. A. Walmsley, Phys. Rev. A **64**, 063815 (2001).
[48] J. G. Pedersen, S. Xiao, and N. A. Mortensen, Phys. Rev. B **78**, 153101 (2008).
[49] J. Grgić, J. G. Pedersen, S. Xiao, and N. A. Mortensen, Photon. Nanostruct. **8**, 56 (2010).
[50] S. Hughes, L. Ramunno, J. F. Young, and J. E. Sipe, Phys. Rev. Lett. **94**, 033903 (2005).
[51] T. P. White and A. A. Sukhorukov, Phys. Rev. A **85**, 043819 (2012).
[52] A. Debnath, K. Debnath, and L. O'Faolain, Opt. Lett. **40**, 193 (2015).
[53] A. F. Oskooi, L. Zhang, Y. Avniel, and S. G. Johnson, Opt. Express **16**, 11376 (2008).
[54] I. B. Udagedara, I. D. Rukhlenko, and M. Premaratne, Phys. Rev. B **83**, 115451 (2011).
[55] K. C. Huang, E. Lidorikis, X. Jiang, J. D. Joannopoulos, K. A. Nelson, P. Bienstman, and S. Fan, Phys. Rev. B **69**, 195111 (2004).
[56] G. Parisi, P. Zilio, and F. Romanato, Opt. Express **20**, 16690 (2012).
[57] S. Ha, A. A. Sukhorukov, K. B. Dossou, L. C. Botten, C. M. de Sterke, and Y. S. Kivshar, Opt. Lett. **34**, 3776 (2009).